



Quantitative phase field simulations of polycrystalline solidification using a vector order parameterTatu Pinomaa ¹, Nana Ofori-Opoku ², Anssi Laukkanen,¹ and Nikolas Provatas³¹*ICME Group, VTT Technical Research Centre of Finland Ltd., Espoo 02044, Finland*²*Computational Techniques Branch, Canadian Nuclear Laboratories, Chalk River, Ontario K0J 1J0, Canada*³*Department of Physics and Centre for the Physics of Materials, McGill University, Montreal, Quebec H3A 2T8, Canada*

(Received 12 February 2021; accepted 21 April 2021; published 24 May 2021)

A vector order parameter phase field model derived from a grand potential functional is presented as an alternative approach for modeling polycrystalline solidification of alloys. In this approach, the grand potential density is designed to contain a discrete set of finite wells, a feature that naturally allows for the growth and controlled interaction of multiple grains using a single vector field. We verify that dendritic solidification in binary alloys follows the well-established quantitative behavior in the *thin interface* limit. In addition, it is shown that grain boundary energy and solute back-diffusion are quantitatively consistent with earlier theoretical work, with grain boundary energy being controlled through a simple solid-solid interaction parameter. Moreover, when considering polycrystalline aggregates and their coarsening, we show that the kinetics follow the expected parabolic growth law. Finally, we demonstrate how this vector order parameter model can be used to describe nucleation in polycrystalline systems via thermal fluctuations of the vector order parameter, a process that cannot be treated consistently with multiphase or multi-order-parameter based phase field models. The presented vector order parameter model serves as a practical and efficient computational tool for simulating polycrystalline materials. We also discuss the extension of the order parameter to higher dimensions as a simple method for modeling multiple solid phases.

DOI: [10.1103/PhysRevE.103.053310](https://doi.org/10.1103/PhysRevE.103.053310)**I. INTRODUCTION**

It is well established that the properties of materials and their performance are ultimately determined by their microstructure. One of the main hallmarks of “microstructure” in materials such as metal alloys is their polycrystalline nature. One of the quintessential goals of materials processing is therefore to understand, predict, and control the polycrystalline structure during the solidification stage of their materials processing. In the last few decades, this task has been more and more undertaken using computational modeling based on so-called multiphase field or multi-order-parameter models [1–3]. The approaches use a discrete set of fields to model different orientations of solids in the liquid, each driven by its own equation of motion that is coupled to diffusion of solutes and/or heat, and interacting with other grains in some phenomenological manner designed into the equations. Such approaches have been very beneficial in pushing the frontiers of computational modeling. However, they also suffer from some limitations in theoretical consistency such as the incorporation of nucleation, thermal fluctuations, orientational invariance, and requiring the use of a large number of fields to simulate polycrystalline materials.

For accurate assessment and prediction of polycrystalline solidification, including nucleation, growth, and grain merging, it is necessary for a simulation approach to have a self-consistent description of the magnitude of the growth kinetics and crystal anisotropy (capillary and kinetic), as well as

a proper description of solute segregation and diffusion. Upon merger of grains, when a cohesive solid network has formed, coarsening ensues, which is dominated by grain boundary migration determined by grain boundary energetics and mobility. Various modeling methods have been developed to study solidification, predict polycrystalline structure formation, and predict the subsequent coarsening.

Cellular automaton and kinetic Monte Carlo methods are two popular techniques that enable large-scale simulations of polycrystalline solidification. However, user intervention is required to properly define the growth kinetics, and these methods are prone to numerical issues and they have considerable limitations in addressing the simulation of alloys and diffusion controlled kinetics of solidification.

The phase field (PF) methodology is typically the most widely used state-of-the-art numerical scheme to describe microstructural solidification. Various PF approaches exist for polycrystalline simulations. One family of models, pioneered by Kobayashi *et al.* [4], Gránásy *et al.* [5], and Warren *et al.* [6], is characterized by the use of both orientation (θ) and order parameter (ϕ) fields (coined $\theta - \phi$ models) to model solidification of any number of crystal orientations. This approach allows for an efficient representation of a large number of grain orientations. It successfully describes basic features of polycrystalline solidification: controllable grain boundary energy versus misorientation, polycrystalline growth, grain merger, and coarsening. However, these models are not without their challenges to implement numerically. Moreover, matched *thin interface* asymptotics has not been performed for

this family of models, and it is likely to be challenging due to the inclusion of singular terms in the model description, e.g., the $|\nabla\theta|$ gradient term in the free energy. Additionally, these models have been shown to exhibit nonphysical topological defects, that have recently been, at least partially, addressed in two-dimensional (2D) simulations [7]. Finally, the extension to three dimensions of this class of models is not immediately straightforward, although some schemes have been explored [8].

Another family of PF models is called MPF models [1]. These deviate from traditional PF models in that the phase field ϕ represents the volume fraction of a phase, which implies that even the liquid is assigned a phase field. As with standard PF models, these models compute the energy of an interface, and anisotropy, by tuning appropriate gradient energy terms [9]. In addition, interaction energy between solid grains includes various polynomial interaction terms between phase fractions. However, MPF models can suffer from non-physical nonlocal adsorption effects due to a complicated free energy landscape wherein the sum of the phase fraction fields must be maintained by a Lagrange multiplier. These need to be eliminated in a somewhat *ad hoc* manner by adding higher order polynomial penalties between phase fraction fields. Also, it is not clear how to integrate thermal fluctuations into the distinct phase fraction fields self-consistently. Another challenge with using MPF models is that, in principle, they nominally require as many fields as there are crystal grains, thus requiring significant computing resources to simulate realistic materials domains. To circumvent this problem requires dynamic grain reassignment algorithms to be implemented [10].

Yet another family of PF models is called multi-order-parameter PF models. As the name suggests, in this class of models, a phase field ϕ maintains the traditional interpretation as a physical order parameter that distinguishes between ordered and disordered states of a crystal. As with MPF models, one order parameter is required for each crystal grain. An earlier approach developed by Ofori-Opoku and Provatas [3] used a quadratic repulsion energy term between order parameters, which is all that is required since this class of models does not suffer from nonlocal adsorption effects. This approach of Ref. [3] allows for a quantitative accounting of solid-liquid interface kinetics and qualitative description of solid-solid interfaces in metals. A weakness with this implementation is that the grain boundary energy cannot be easily tuned, resulting in grain boundary energies corresponding to high angle or high energy grain boundaries. As with MPF models, for multi-order-parameter models the Langevin noise based nucleation is problematic to implement when multiple order parameters are fluctuating in the same material point due to the use of polynomial (here quadratic) repulsive interaction terms.

In this paper, we present an alternative phase field modeling scheme to describe solidification and coarsening of multiple crystallographic orientations in the context of a physical order parameter description. We accomplish this by adopting a two-dimensional vector order parameter model as in Ref. [11], which is then integrated with a previous quantitative modeling scheme for solidification based on a grand potential energy functional [12]. This main innovations of this

approach are the trivial generation of a Landau free energy landscape corresponding to any number of discrete orientations in the context of a *single* physical order parameter field, simple control of grain boundary energy, and self-consistent incorporation of thermal fluctuations into dynamical simulations.

The paper is organized as follows. In Sec. II, we introduce the vector order parameter model and review its parametrization. Section III examines the model's ability to reproduce some important benchmarks quantitatively. These include free solidification of a single dendrite, grain boundary energy, grain merger and back-diffusion, grain growth and coarsening, grain boundary segregation in polycrystalline growth, and noise-induced nucleation. Section IV further discusses the properties of the model and its extensions to multiple phases and higher dimensions. We conclude in Sec. V.

II. METHODOLOGY

This section develops the formalism of the vector phase field model. In this paper, the focus is to demonstrate the properties of this phase field methodology, and so for simplicity we limit ourselves to binary alloys. We will formulate the model formally in the grand potential ensemble, meaning that the dependent fields are the order parameter and the chemical potential. We begin by describing the grand potential energy functional, highlighting its vectorized Landau landscape. Following this, we discuss the dynamics of the vector order parameter and the chemical potential. We then highlight the parameter relations necessary to achieve quantitative correspondence with the sharp interface model of solidification.

A. Grand potential functional

We start by defining a vector order parameter defined as $\vec{\phi}(\vec{x}, t) = (\phi_X(\vec{x}, t), \phi_Y(\vec{x}, t))$. We also project $\vec{\phi}$ into polar coordinates R and θ according to

$$\phi_X = R \cos(\theta), \quad (1)$$

$$\phi_Y = R \sin(\theta), \quad (2)$$

where R can be interpreted as the “traditional” solid-liquid order parameter, and θ is an additional degree of freedom that is used to design a Landau functional the bulk part of which contains a discrete number of solid wells. This is given by

$$f_{\text{Landau}}(R, \theta) = R^2 - 2 \frac{1 + b \cos(N_{\text{wells}}\theta)}{1 + b} R^3 + R^4, \quad (3)$$

where N_{wells} sets the number of discrete solid wells corresponding to unique crystalline orientations, and b controls the free energy barrier between neighboring solid wells. Equation (3) is usually referred to as the “double well potential” in conventional PF models, where there is one solid well and one liquid well. An example of the Landau landscape is shown in Fig. 1 with $N_{\text{wells}} = 8$ and $b = 0.05$. Our approach is analogous to Morin *et al.* [11], who used a different order polynomial in R to describe the Landau free energy function (polynomial orders R^n , $n = 2, 4, 6$). Here, we modify their approach to a polynomial which is a natural extension of the single order parameter PF models typically used for solidifi-

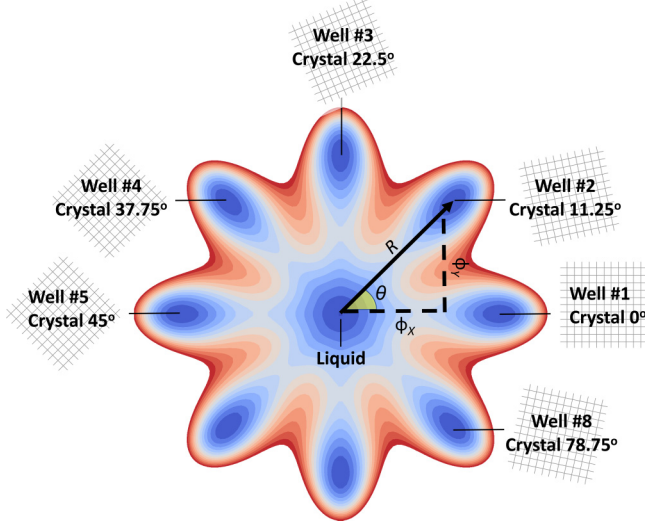


FIG. 1. Landau free energy landscape in the space of a vector order parameter with $N_{\text{wells}} = 8$ and a solid-solid interaction strength parameter $b = 0.05$. The energy minimum in the center corresponds to the liquid well, while each of the N_{wells} correspond to a distinct solid orientation. In this paper, the dynamics of the order parameter are written in term of its Cartesian projections $\phi_x = R \cos(\theta)$ and $\phi_y = R \sin(\theta)$.

cation, thus adopting polynomial orders of R^n , $n = 2, 3, 4$. It is noted that for 2D cubic lattices, the physical crystalline orientation is one fourth of the Landau angle θ . This is illustrated in Fig. 1. Thus, for example, $\theta = \pi$ (180°) corresponds to the maximum crystal misorientation, which for a cubic 2D lattice is $\pi/4$ (45°).

To the multiwell function in Eq. (3) we add a chemical energy contribution of the form

$$\omega_{\text{ch}}(\mu, R) = P(R) \omega^s(\mu, T) + [1 - P(R)] \omega^\ell(\mu, T), \quad (4)$$

where $\mu = \mu(\vec{x}, t)$ is the chemical potential field; ω^s and ω^ℓ are the grand potential densities of the solid and liquid phases, respectively; and $P(R)$ interpolates the thermodynamic potentials across bulk states. It satisfies $P(0) = 0$ and $P(1) = 1$. Equation (4) provides the chemical driving force for solidification written in terms of the chemical potential, which is the natural thermodynamic variable of the grand potential functional.

The last contribution to the grand potential energy comprises gradient energy terms required to account for nonlocal interactions. In terms of the Cartesian representation of the order parameter, we also define the gradient interaction term as according to

$$f_{\text{int}} = \frac{1}{2} W_X^2 |\nabla \phi_X|^2 + \frac{1}{2} W_Y^2 |\nabla \phi_Y|^2, \quad (5)$$

where $\{W_X, W_Y\}$ can be shown to be proportional to gradient energy and inversely proportional to the square root of the nucleation barrier [13]. The coefficients must be made anisotropic in order to self-consistently reproduce the symmetries of crystal growth in solidification. The anisotropy of these coefficients will be discussed further below.

Combining Eqs. (3), (4), and (5) yields a grand potential functional of the form

$$\begin{aligned} \frac{1}{H} \Omega[\vec{\phi}, \mu, T] = & \int_V \left(\frac{1}{2} W_X^2 |\nabla \phi_X|^2 + \frac{1}{2} W_Y^2 |\nabla \phi_Y|^2 \right. \\ & + R^2 - 2 \frac{1 + b \cos(N_{\text{wells}} \theta)}{1 + b} R^3 + R^4 \\ & + \frac{1}{H} P(R) \omega^s(\mu, T) \\ & \left. + \frac{1}{H} [1 - P(R)] \omega^\ell(\mu, T) \right) dV, \quad (6) \end{aligned}$$

where H is the nucleation barrier, T is the temperature, and $P(R)$ is a function that interpolates the grand potential between its bulk solid to liquid values. An explicit form of $P(R)$ that we use in this paper is the one introduced by Wheeler, Boettinger, and McFadden [14], namely, $P(R) = 10R^3 - 15R^4 + 6R^5$, although several other forms are possible.

B. Phase field dynamics

The dynamical evolution for the vector order parameter is governed by dissipative relaxation dynamics in each component field, while solute evolution follows the usual mass conservation dynamics. The explicit dynamical equations for these fields are given by

$$\frac{\partial \phi_K}{\partial t} = - \frac{\partial \Omega}{\partial \phi_K} + \eta_K, \quad K = \{X, Y\}, \quad (7)$$

$$\frac{\partial c}{\partial t} = \nabla \cdot [M(\vec{\phi}, c) \nabla \mu], \quad (8)$$

where $K = \{X, Y\}$ denote the two components of $\vec{\phi}$, η_K are noise sources in each component (discussed further below), while $c(\vec{x}, t)$ is the solute concentration field of a binary alloy, which in the grand potential ensemble is determined via the chemical potential field $\mu(\vec{x}, t)$ according to the relation

$$c = - \frac{\delta \Omega}{\delta \mu} = P(R) c^s(\mu) + [1 - P(R)] c^\ell(\mu), \quad (9)$$

where $c^s = \partial \omega^s / \partial \mu$ and $c^\ell = \partial \omega^\ell / \partial \mu$. Equation (9) can be seen as a constraint between c and μ . Combining Eq. (9) with Eq. (8) yields the following evolution equation for $\mu(\vec{x}, t)$ directly:

$$\chi(\mu) \frac{\partial \mu}{\partial t} = \nabla \cdot [M(\vec{\phi}, c) \nabla \mu] - P'(R) [c^s(\mu) - c^\ell(\mu)] \frac{\partial R}{\partial t}, \quad (10)$$

where the susceptibility field $\chi[\mu(\vec{x}, t)]$ is given by

$$\chi = P(R) \frac{\partial c^s(\mu)}{\partial \mu} + [1 - P(R)] \frac{\partial c^\ell(\mu)}{\partial \mu}. \quad (11)$$

Either Eq. (10) or Eq. (8) can be coupled to the order parameter component dynamics of Eq. (7).

In what follows, we will be focusing on examining the efficiencies and self-consistencies afforded when using a vector order parameter in favor of multiple scalar order parameters or phase fractions in phase field modeling. As a result, we will limit the system studied to a dilute binary alloy. We will simulate phase field dynamics using Eqs. (8) and (7). Furthermore, in order to achieve quantitative solidification results in the

limit of a diffuse interface, we will incorporate an antitrapping flux in Eq. (8), the role of which is to suppress spurious kinetic behavior caused by the use of a diffuse interface [15,16]. It is noted that the dynamical evolution equation for mass transport no longer follows a variational formulation when antitrapping is used.

Taking into account the above considerations, we proceed as follows to arrive at an evolution equation for the vector order parameter components of our model: first we substitute the grand potential densities for the solid and liquid phases of an ideal binary alloy into Eq. (6); secondly, we carry out the variational derivatives as specified in the first of Eqs. (7); thirdly, we simplify the chemical driving force analogously to Ref. [12]. This yields

$$\begin{aligned} \tau_K \frac{\partial \phi_K}{\partial t} = & \nabla \cdot \left(\frac{\partial f_{\text{int}}}{\partial (\nabla \phi_K)} \right) - \frac{\partial f_{\text{int}}}{\partial \phi_K} + (2 + 3R - 4R^2) \phi_K \\ & + 6 \frac{b(\cos(N_{\text{wells}}\theta) - 1)}{1 + b} R \phi_K \\ & + 2bN_{\text{wells}} \frac{\sin(N_{\text{wells}}\theta)}{1 + b} R \frac{\partial \theta}{\partial \phi_K} \\ & - \frac{\lambda}{1 - k_e} \left(e^u - 1 - \frac{T_\ell - T}{|m_\ell^e|c_0} \right) (1 - R)^2 \phi_K \\ & + \eta_K \text{ for } K \in \{X, Y\}, \end{aligned} \quad (12)$$

where u is a dimensionless chemical potential difference relative to the equilibrium chemical potential for a binary alloy, expressed in terms of concentration as $u = \ln(c/\{c_0[1 - (1 - k_e)R]\})$ [13]. The first two terms on the right-hand side of Eq. (12) represent the interface energy penalty, the expressions of which are rather lengthy, and are thus shown in the Appendix. The parameter τ_K is the anisotropic time constant; λ is the coupling constant, which is used to control the model's convergence onto the key results of the sharp interface model; and k_e is the equilibrium partition coefficient. We have also tacitly appended into the chemical driving force of Eq. (12) a temperature component, where T_ℓ is the liquidus temperature, T is the local temperature, m_ℓ^e is the liquidus slope, and c_0 is a reference alloy concentration. The last term in Eq. (12), η_K , is thermal noise, discussed further below.

The concentration evolution follows from Eq. (8) and maps identically onto the dilute binary alloy model of Refs. [15,16], with R replacing the solid-liquid order parameter, but where R is scaled here to the limits $[0,1]$. Explicitly, the concentration equation becomes

$$\begin{aligned} \frac{\partial c}{\partial t} = & \nabla \cdot \left[\{h(R)D_S k_e + D_\ell[1 - h(R)]\} \nabla e^u \right. \\ & \left. + W_0 a_t c_0 (1 - k_e) e^u \frac{\partial R}{\partial t} \frac{\nabla R}{|\nabla R|} \right], \end{aligned} \quad (13)$$

where $h(R) = R$ is an interpolation function, D_S (D_L) is the solute diffusion coefficient in solid (liquid), and a_t is the antitrapping current prefactor. Its value is listed in Table I and is determined by conducting a matched asymptotic analysis using the methods in Refs. [13,16].

A key feature of quantitative phase field modeling is the use of matched interface asymptotic analysis to determine

TABLE I. Phase field model parameters for Al-4.5 at. % Cu.

Partition coefficient k_e	0.15
Liquidus slope m_ℓ^e	-5.3 K/wt %
Alloy concentration c_0	4.5 at. %
Gibbs-Thomson coefficient Γ	2.41×10^{-7} K m
Solutal capillary length d_0	12.17 nm
Liquid free energy curvature $g_{e,c}^\ell$	9.05×10^9 J/m ³ ^a
Liquid diffusion coefficient D_ℓ	4.4×10^{-9} m ² /s
Solid diffusion coefficient D_S	0 or 4.4×10^{-11} m ² /s ^b
Kinetic coefficient β	0.0 s/m
Capillary anisotropy strength ϵ_c	0.02
Interface width W_0	$d_0/0.277$
Asymptotics constant a_1	7.07107
Asymptotics constant a_2	0.078337
Asymptotics constant a_t	$1/\sqrt{2}$
Mesh spacing Δx	$0.1W_0, 0.2W_0,$ and $0.6W_0$ ^c
Time step size Δt	$0.8 \Delta x^2/(6D_\ell)$

^aValue from the Thermo-Calc TCAL database.

^b D_S is nonzero only for back-diffusion analysis in Fig. 5.

^cWe use different Δx depending on the sections: $\Delta x = 0.6W_0$ for the single crystal solidification benchmark (Sec. III B), $\Delta x = 0.1W_0$ for one-dimensional grain boundary analyses (Sec. III C), and $\Delta x = 0.2W_0$ for polycrystalline simulations (Secs. III D and III E).

the parameter relations that allow the model to emulate the interfacial kinetics of the classical sharp interface model of solidification. There have been several important works on this topic for models using a scalar order parameter [13,16–18]. The outcomes are similar; they lead to relationships between microscopic phase field parameters (τ_0 , W_0 , and λ) and the macroscopic material parameters of the sharp interface model, namely, the capillary length (d_0) and kinetic coefficient (β).

It turns out that we can directly apply the aforementioned matched asymptotic analysis methods, developed for scalar order parameter PF models, in order to inter-relate the parameters τ_K , W_K , and λ in our model. The rationale in doing so is as follows: if we ignore anisotropy (as is done in the above-referenced approaches) and only consider single individual order parameter profiles going from the liquid well into any of the solid wells of our model (see Fig. 1), we can map $\tau_K \rightarrow \tau_0$ and $W_K \rightarrow W_0$. Further, in this situation, the Landau angle variable becomes a constant everywhere, equal to $\theta = m2\pi/N_{\text{wells}}$ where m is an integer. This guarantees the elimination of the cubic terms in the Landau contribution to the energy. This reduces Eq. (12) identically to the traditional form of the scalar order parameter evolution equation in both order parameter components, ϕ_K , $K = X, Y$. As a result, the matched interface asymptotics in Refs. [13,16,18] is exactly applicable. It should be noted that this assumes that the order parameter profile can “ride the rails” along a line between the liquid well to any of the solid wells. This is easily satisfied, and any error is negligible in our single crystal benchmark tests presented in the Sec. III B. These considerations lead to the following relations:

$$d_0 = a_1 \frac{W_0}{\lambda}, \quad (14)$$

$$\beta = a_1 \frac{\tau_0}{\lambda W_0} \left[1 - a_2 \frac{\lambda W_0^2}{\tau_0 D_\ell} \right], \quad (15)$$

where a_1 and a_2 are asymptotic analysis constants listed in Table I, where it is notable that solid-liquid ordering is in the interval $[0,1]$, while perhaps a more common practice is to scale the order parameter for the interval $[-1, 1]$.

To make the model anisotropic, the phase field parameters W_K and τ_K are appended with an anisotropy correction according to $W_K = W_0 a_K(\phi_X, \phi_Y)$, and assuming that $\beta = 0$, $\tau_K = \tau_0 a_K(\phi_X, \phi_Y)^2$ (assuming $\beta = 0$), where a_k is an anisotropy function. For 2D cubic crystals, a_k is defined by

$$a_K(\phi_X, \phi_Y) = 1 + \epsilon_c \cos(4\theta_{\nabla\phi_K} - \theta), \quad K \in \{X, Y\}, \quad (16)$$

where ϵ_c is the anisotropy strength. It should be noted that in Eq. (16) the Landau angle θ is not multiplied by 4 to achieve the correct rotation for a cubic 2D lattice, as visualized in Fig. 1. Here, $\theta_{\nabla\phi_K}$ is the local solid-liquid interface normal angle for vector order parameter component ϕ_K ($K \in \{X, Y\}$), given by

$$\theta_{\nabla\phi_K} = \arctan\left(\frac{\partial_y \phi_K}{\partial_x \phi_K}\right), \quad K \in \{X, Y\} \quad (17)$$

where θ sets the reference Landau angle, i.e.,

$$\theta = \arctan\left(\frac{\phi_Y}{\phi_X}\right). \quad (18)$$

The last term, η_K for $K \in \{X, Y\}$, represents thermal fluctuations, which must satisfy the fluctuation-dissipation theorem in order to assure convergence of the phase field equations to thermodynamics equilibrium. We follow the approach given in Ref. [19] to scale these noise sources quantitatively, which yields

$$\begin{aligned} \langle \eta_K, \eta_K \rangle &= 2k_B T \frac{1}{H\tau_0} \delta(\mathbf{x} - \mathbf{x}') \delta(t - t') \\ &= 2k_B T \frac{1}{\tau_0} \frac{a_1 W_0}{J d_0} \frac{1}{c_0^2 g_{c,c}^\ell} \frac{1}{\Delta x^3} \frac{1}{\Delta t}, \end{aligned} \quad (19)$$

where k_B is Boltzmann's constant. On the second line we approximate the delta functions by Δx and Δt following Ref. [19]. Furthermore, in the second line of Eq. (19), we substituted H with an expression from the matched interface asymptotics for dilute binary alloys [13,16], where $J = 1/30$ is a scaling factor (specific to the interpolation function we use for the driving force), and $g_{c,c}^\ell$ is the liquid free energy curvature. In addition, the noise term in Eq. (19) is filtered in space and time so that the fluctuations occur approximately in the length scale of W_0 and time scale τ_0 , as these can be considered as the smallest physical scales in solidification that the current phase field model can resolve. More details about this filtering scheme can be found in the Supplemental Material [20].

C. Alternate gradient formulation

Following Morin *et al.* [11], we chose a gradient energy penalty in Eq. (5) that is a sum of the contributing components, but our coefficients are made anisotropic to satisfy a crucial criterion required for solidification of metals. Another perhaps more consistent choice would be to represent the energy penalty in terms of polar coordinates R and θ ,

in the form

$$\frac{1}{2} W^2 |\nabla R|^2 + \frac{1}{2} W^2 R^2 |\nabla \theta|^2. \quad (20)$$

While this form reproduces some features of solidification and coarsening qualitatively, this $R - \theta$ representation suffers from lattice pinning due to topological defects, analogous to those seen in the orientation PF models [7]. Furthermore, it is unclear how to implement thermodynamically consistent noise for the θ field in our vector order parameter model. As such this alternate formulation is not considered further in this paper and will be pursued in future work.

III. MODEL BENCHMARKS

In this section we demonstrate that our vector order parameter model reproduces certain established benchmark results of solidification and solid-state coarsening phenomena. In particular, we first analyze single crystal dendrite growth kinetics. We then conduct an analysis of grain boundary profiles, their energies, and their coalescence. Following this, we verify that the polycrystalline coarsening for model A dynamics (i.e., no concentration diffusion) is consistent with theoretical expectations. Finally, we demonstrate nucleation and growth of a polycrystalline alloy system using thermal noise fluctuations of the vector order parameter.

A. Numerical implementation

All phase field simulations we present are performed using the computational platform presented in Ref. [21], which contains adaptive mesh refinement and distributed memory parallelization based on MPI.

Concentration evolution in Eq. (13) was implemented using a finite volume method, as well as the divergence terms in the order parameter equations of Eq. (12). Other gradient terms were expressed via simple five stencil finite differencing. Neumann, i.e., zero flux, boundary conditions were applied, unless otherwise stated. We use forward Euler time integration, where it noted that the forward Euler time step of the stochastic noise term η_K in Eqs. (12) and (19) is proportional to $\sqrt{\Delta t}$.

B. Convergence analysis for dendritic solidification

Since our vector order parameter model relies on the same diffuse interface analysis as Refs. [15,16], we verified that its dynamics reproduces the dendritic solidification results predicted by the classical sharp interface model of solidification. To do so, we initialized a seed with radius $22d_0$ in a uniform supersaturation $\Omega = c/\{c_0[1 - (1 - k_e)R]\} = 0.55$. We then performed a reference simulation using the scalar order parameter model presented in Ref. [15] and compared it to a simulation conducted with our model with $N_{\text{wells}} = 8$ and a solid-solid interaction barrier parameter $b = 4.0$. We set $W_0 = d_0/0.277$ and $\Delta x = 0.6W_0$ in our simulations.

The solid seed is initialized into the second well of our Landau energy landscape (well 2 in Fig. 1), which corresponds to a crystalline rotation of 11.25° relative to the x axis. We applied the same lattice rotation to the standard phase field model of Karma [15]. The resulting dendrite morphology and centerline concentration through to the dendrite tip

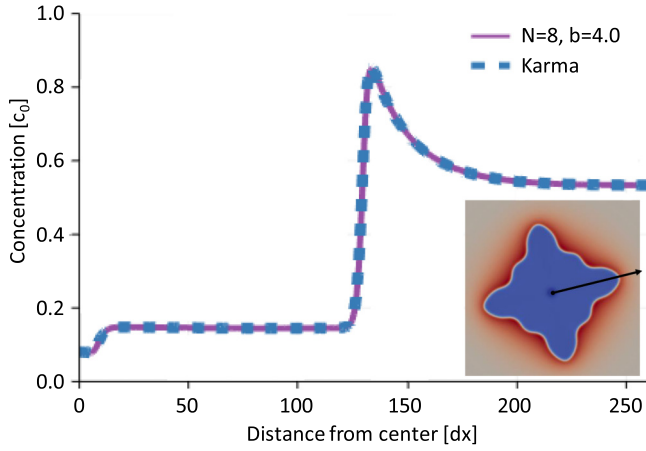


FIG. 2. Binary alloy dendrite growth benchmark and centerline concentration computed with the scalar PF model of Ref. [15] (dashed line) compared to the corresponding result from the vector order parameter model with $N_{\text{wells}} = 8$ and $b = 4.0$ (solid line). In both cases, the grain is rotated 11.25° , $W_0 = d_0/0.277$, the initial seed radius is $22d_0$ and the initial supersaturation $\Omega = 0.55$. Bottom right inset: Dendrite solute contours. The profiles are recorded at time $t = 480\tau_0$.

are shown in Fig. 2 at a time $t = 480\tau_0$. The results show excellent agreement between the standard scalar order parameter alloy model and our vector order parameter model. It is noted that these results do not change with a decrease of the solid-solid barrier parameter to $b = 0.1$. We also verified that the tip speeds are indistinguishable from the benchmark data (not shown here). It is noted that an excessively large interaction parameter b leads to unphysical oscillations inside the solid. These can be suppressed by decreasing Δt . Thus, for $N_{\text{wells}} = 8$, simulations with $b = 0.1$ are stable for $\Delta t = 0.8\Delta x^2/(6D_\ell)$, while, for $b = 4.0$, $\Delta t = 0.4\Delta x^2/(6D_\ell)$ is required to maintain stability.

C. One-dimensional grain boundary analysis

This subsection analyzes grain boundaries and their energy in the context of the vector order parameter model. We perform simulations in one spatial dimension to model a one-dimensional (1D) grain boundary analysis using so-called model A dynamics, i.e., only the vector order parameter evolution of Eq. (12) is considered, while the concentration dynamics in Eq. (13) is switched off.

We applied a fixed value boundary condition so that the far ends of the 1D grain boundary geometry satisfy $\phi_x^2 + \phi_y^2 = 1$, and such that $\theta = \arctan(\phi_y/\phi_x)$ corresponds to the appropriate crystal orientations. The grid spacing was set to $\Delta x = 0.1W_0$, even though $\Delta x = 0.2W_0$ also yields convergent results. It was noted that the use of larger grid spacing, such as $\Delta x = 0.5W_0$, may lead to lattice pinning in the multidimensional polycrystal coarsening simulations, which are discussed in Sec. III D. Grain boundary equilibration was conducted by initializing two 1D “solid blocks” corresponding to two different solid wells, with hyperbolic tangent tails overlapping at $R = 0.5$. Approximately 20 000 time steps were required to equilibrate the profiles into a static grain boundary.

The final equilibrium profiles were found to be independent of the details of the profile initialization.

The resulting profiles are shown in Fig. 3 for a solid-solid barrier parameter $b = 4.0$ and 0.1 , along with the corresponding vector order parameter trajectories defining each grain boundary in the Landau free energy landscape (superimposed as a black solid line). For each choice of b , the driving force was set to either zero, i.e., $\Delta := (T_l - T)/[(1 - k_e)|m_l^e|c_0] = 0$, or $\Delta = 0.55$. In all cases, solid-liquid ordering, represented by R , develops a typical cusplike morphology in the grain boundary region consistent with earlier polycrystalline PF models, such as in orientation field models [7]. Moreover, the solid-solid grain boundary ordering decreases as the misorientation increases, approaching a “wet” grain boundary at high misorientation, as expected. The use of a smaller solid-solid barrier parameter $b = 0.1$ increases the ordering at the grain boundary, which is consistent with a smaller energy barrier between the solid wells. Finally, applying a driving force ($\Delta = 0.55$) increases the ordering at the grain boundary as expected.

In Fig. 3(d), one can see slight oscillations in the solid-liquid ordering across the grain boundaries GB1,3 and GB1,6. This is expected for the small solid-solid barrier coefficient ($b = 0.1$) and large quench ($\Delta = 0.55$), as it is energetically favorable for the order parameter profile to approach the intermediate solid well, as shown in the grain boundary trajectories (black lines) in Fig. 3(d). Curiously, this type of solid-liquid ordering oscillation is also found in phase field crystal simulations of Mellenthin *et al.* [22]. However, we expect that these solid-liquid ordering oscillations are uncommon for metals and should be generally avoided by setting the solid-solid barrier to a sufficiently large value, especially when the computational interface width W_0 is increased to thin interface conditions.

We next evaluated grain boundary energies, the results of which are shown in Fig. 4. The grain boundary energy is defined as the excess energy at the interface, which for 1D systems can be shown to have the form

$$\begin{aligned} \gamma_{\text{GB}} = \int_{-\infty}^{\infty} \left\{ \frac{1}{2} \epsilon_0^2 \left[\left(\frac{\partial}{\partial x} \phi_x \right)^2 + \left(\frac{\partial}{\partial x} \phi_y \right)^2 \right] \right. \\ \left. + H \left(R^2 - \frac{1 + b \cos(N_{\text{wells}} \theta_\phi)}{1 + b} R^3 + R^4 \right) \right. \\ \left. + P(R) \Delta \right\} dx, \end{aligned} \quad (21)$$

where

$$\begin{aligned} \frac{1}{H} &= a_1 \frac{W_0}{d_0} \frac{1}{c_0^2 g_{c,c}^\ell}, \\ \epsilon_0 &= W_0 \sqrt{H}, \\ \Delta &= \frac{T_l - T}{(1 - k_e) |m_l^e| c_0}. \end{aligned} \quad (22)$$

For an ideal amorphous grain boundary, an estimate of the energy can be derived analytically; the details are provided in the Supplemental Material [20]. An ideal amorphous grain boundary assumes that the Landau angle θ is constant except at the center of the grain boundary, where the ordering goes to zero. Without a driving force ($\Delta = 0$), this energy has a

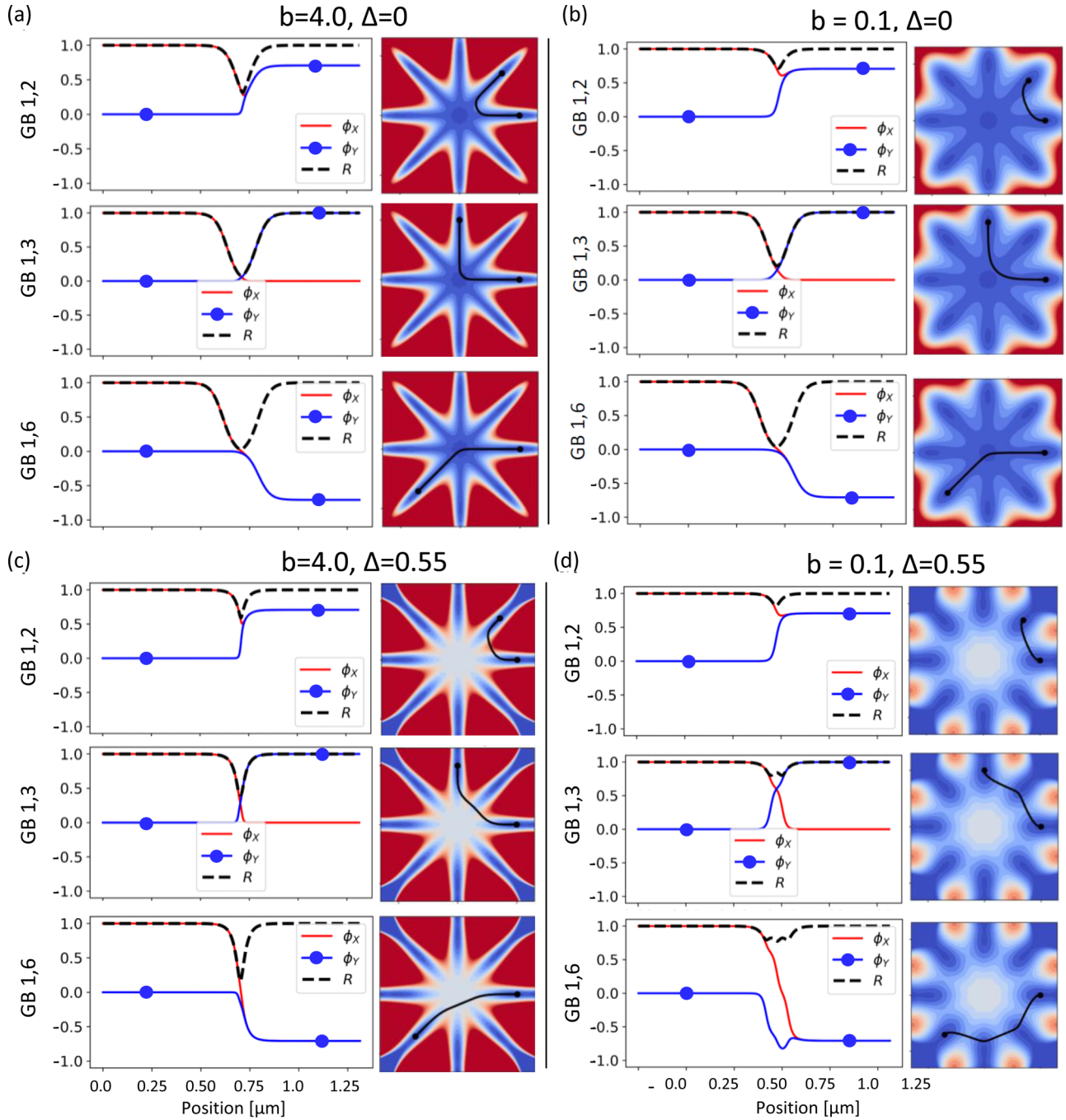


FIG. 3. Grain boundary profiles and vector order parameter trajectories in Landau landscapes with zero driving force $\Delta = 0$ (a, b) and a relatively large driving force $\Delta = 0.55$ (c, d). Two different solid-solid barrier heights are considered ($b = 0.1$ and 0.4). Concentration dynamics are not considered here.

closed-form expression that is twice the solid-liquid interface energy given by

$$\gamma_{\text{GB}}^{\text{amorph}} = 2\gamma_{\text{SL}} = \frac{W_0 H}{\sqrt{3}} \approx 0.44 \text{ J/m}^2, \quad (23)$$

where parameters are taken from Table I. When an undercooling (here $\Delta = 0.55$) is applied, the grain boundary energy needs to be numerically computed, yielding $\gamma_{\text{GB}}^{\text{amorph}}(\Delta = 0.55) \approx 1.31 \text{ J/m}^2$ (see the Supplemental Material [20] for more details). These estimated grain boundary energies

($\gamma_{\text{GB}}^{\text{amorph}}$) provide ideal limits for comparison and are shown as horizontal lines in Fig. 4. These energies are compared for the model A equilibrated grain boundary profiles shown in Fig. 3, where the excess grain boundary energies are calculated by numerically evaluating Eq. (21), and the resulting energies are shown by the scatter data in Fig. 4.

The grain boundary energies obtained from our model are in good agreement with previous phase field crystal simulations of Mellenthin *et al.* [22], which are characterized by three main features. First, without a driving force (filled

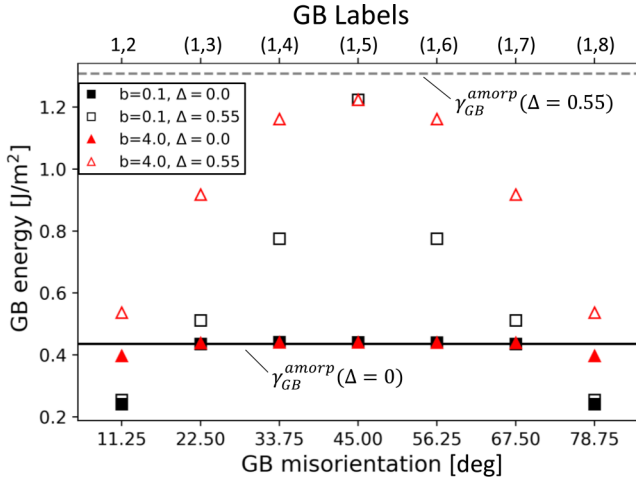


FIG. 4. Grain boundary energy vs grain boundary misorientations for the case of $N_{\text{wells}} = 8$. Grain boundaries were grown with model A dynamics (no concentration dynamics) for two values of undercooling, $\Delta = 0$ or 0.55 . For each, two values of the solid-solid barrier parameter were used, $b = 0.1$ or 4.0 . Analytical grain boundary energies, $\gamma_{\text{GB}}^{\text{amorph}}(\Delta)$, are shown as horizontal lines, where the solid line corresponds to $\Delta = 0$ and the dashed line corresponds to $\Delta = 0.55$.

markers in Fig. 4), the smallest misorientations (up to misorientation $\approx 11.25^\circ$), produce slightly attractive grain boundaries. Second, large misorientations up to the symmetry point for cubic crystals lead to grain boundary energies identical to the ideal grain boundary energy, corresponding to zero applied driving force [$\gamma_{\text{GB}}^{\text{amorph}}(\Delta = 0)$]. Third, adding a driving force of $\Delta = 0.55$ (hollow markers in Fig. 4) increases the grain boundary energy in a gradual manner as a function of misorientation. Overall, this vector order parameter model produces low-angle (attractive) and high-angle (repulsive) grain boundaries which are in good agreement with phase field crystal simulations of Mellenthin *et al.* in terms of grain boundary energy versus misorientation versus undercooling.

As expected, an increase in solid-solid barrier parameter b leads to a corresponding increase in grain boundary energy for all cases, except for those cases where the energy has already saturated to its limiting value, i.e., when the grain boundary has saturated to a large misorientation (for $\Delta = 0$ this corresponds to misorientations 22.50 – 45° and their corresponding crystalline symmetric values, while for $\Delta = 0.55$ a similar saturation is not found).

When we consider a thermodynamic driving force applied to the grain boundary, the simulated model A energies at the maximum misorientation are smaller than our analytical estimate (dashed horizontal line in Fig. 4). This discrepancy is due to the fact that in the analytical estimate we assume that solid-liquid order is zero in the grain boundary region, and that θ varies only at zero ordering, neither of which is well satisfied (nor to be expected) for $\Delta = 0.55$, particularly for small b ($b = 0.1$), which, as discussed above, leads to small interfacial oscillations within the interface.

Grain boundary back-diffusion

This subsection demonstrates that solute evolution leading to the development of cohesive solid networks and grain boundaries follows behavior consistent with the seminal work of Rappaz *et al.* [23]. For this part of the paper, we activate the concentration dynamics of Eq. (13), and apply a constant cooling rate 2×10^5 K/s. In addition, we allow for enhanced back-diffusion by assuming that the solid diffusion coefficient is $D_s = D_\ell/100$. Here, the two solid regions were initialized with a thick liquid layer in between them to emulate, in one dimension, the conditions of grain-grain merger during solidification.

Back-diffusion was simulated in this grain boundary system having the smallest misorientation allowed by our model (labeled GB 1,2 in Fig. 4), corresponding to a misorientation of 11.25° . The data were collected at two solid-solid barrier parameters, $b = 0.1$ and 4.0 . The snapshots of the phase field profiles and the corresponding concentration profiles are shown in Fig. 5(a), where time increases from top to bottom. Figure 5(b) plots the peak grain boundary concentration as a function of time superimposed on the dilute Al-Cu phase diagram. At early times, when the tails of the two grains are not in contact, the concentration follows the liquidus line. As the two grains begin to “feel” one another through their order parameter tails, and start to interact, the concentration starts to drop towards the solidus concentration. Due to back-diffusion, they asymptotically start to approach the average alloy concentration (vertical dashed line). This behavior is consistent with the back-diffusion results reported by Rappaz *et al.* [23] and Ofori-Opoku and Provatas [3]. Using a large solid-solid barrier parameter, $b = 4.0$ [red circles in Fig. 5(b)], decreases the solid-solid ordering around the grain boundary for a given undercooling, and thereby increases the concentration peak, as expected.

Overall, the above 1D grain boundary back-diffusion study shows the expected behavior in terms of solid-solid ordering, grain boundary energy behavior, grain boundary merger, and solute distribution at the grain boundary. It is also noteworthy that the properties reproduced by the proposed vector order parameter model have also all been exhibited by the more fundamental phase field crystal model, as documented in Ref. [22], as well as in more traditional phase field models [3,23].

D. Polycrystalline grain coarsening

In this subsection, we verify that the model A dynamics of the proposed vector order parameter model satisfies the theoretically established $\approx t^{1/2}$ coarsening kinetics. For this paper, we set the grid size $\Delta x = 0.2W_0$ as we found that a larger value of mesh size (e.g., $\Delta x = 0.5W_0$) can lead to lattice pinning, especially when a large driving force is applied. Simulations were performed using a driving force $\Delta = 0.55$ and an interaction barrier strength of $b = 4.0$, and we applied zero gradient boundary conditions. For this study, we initialized the simulation domain with a random Voronoi tessellation with full ordering $R = \phi_x^2 + \phi_y^2 = 1$ within the bulk of each grain, as shown in the first column of Fig. 6(a). The other columns of Fig. 6(a) show the time evolution and grain coarsening in the polycrystalline system, where each row highlights different

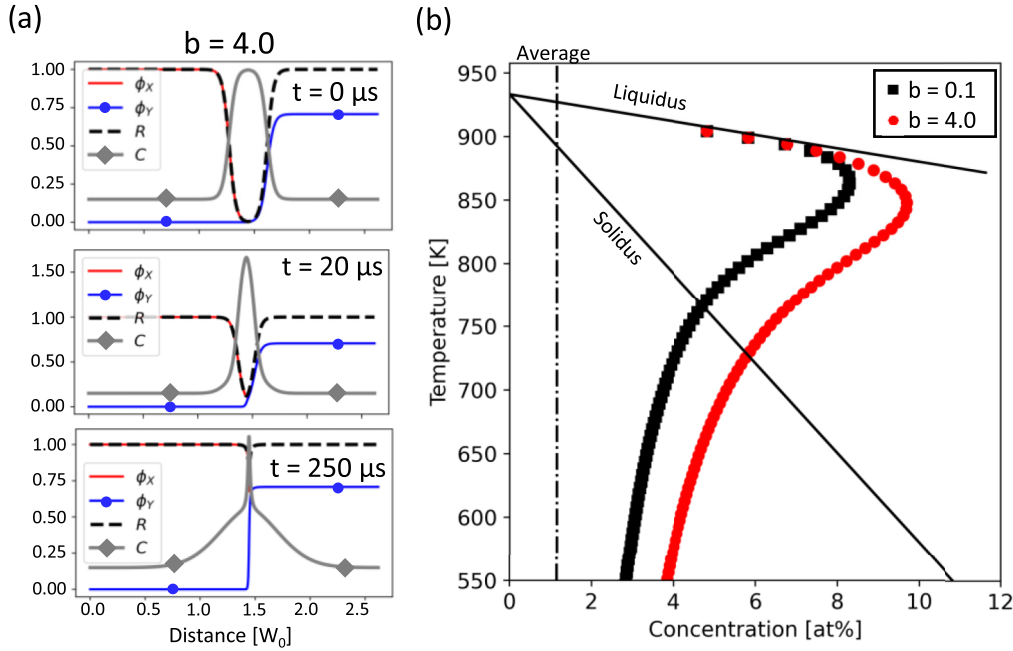


FIG. 5. Grain boundary coalescence for a cooling rate 10^6 K/s, showing the evolution of the corresponding order parameter and concentration profiles. (a) Solid-liquid ordering and concentration at three time steps for $b = 4.0$, where concentration (C) is in units of the average composition $c_0 = 4.5$ at. % Cu. (b) Grain boundary peak concentration at various time steps for $b = 0.1$ and 4.0 .

measures of the vector order parameter. It is noteworthy that the regions corresponding to high-angle grain boundaries lead to the emergence of solid-liquid ordering.

To verify that the grain coarsening follows the well-known results of linear (parabolic) growth with area (radius) versus time, we evaluated the average grain size using the so-called intercept method, which is typically used in experimental settings to determine grain sizes. In this method, a line is drawn randomly across the microstructure and the size of the grains intercepting this line is measured. A sufficiently large number of these line-based measurements, at various orientations through the microstructure data, leads to a good estimate of the grain size d_{grain} . We converted the so-calculated average grain size to an equivalent circle via $\pi(d_{\text{grain}}/2)^2$. The grain area versus time is shown in Fig. 6(b). Mean-field arguments, stating that grains grow by mean curvature, dictate that the grains should coarsen such that the average grain area increases linearly with time. This linear coarsening regime can be seen in Fig. 6(b), where a dashed line is drawn as a guide for the eye for the linear regime. As the grain size approaches the system size, the mean field assumption breaks down and the scaling relation no longer holds.

E. Nucleation and polycrystalline solidification in an alloy

This subsection demonstrates noise-induced nucleation and polycrystalline solidification in a binary alloy using the proposed vector order parameter model. The aim here is to highlight the robustness of the model and the self-consistency of applying thermal noise acting on the vector order parameter defined everywhere. To prevent interference with the evolution of existing ordered crystals, we threshold the noise terms such that it is only active in the vicinity where $R =$

$\sqrt{\phi_x^2 + \phi_y^2} < 0.9$. We additionally filter the noise in space and time, so that the fluctuations occur roughly over a length scale of W_0 (not Δx), and over the time scale τ_0 (not Δt). The details of these filtering procedures are given in the Supplemental Material [20]. These filtering procedures were necessary to ensure the numerical stability of the system, and since fluctuations below the length and time scales (W_0 and τ_0) have no clear physical meaning in coarse grained field theories. For the simulations shown in this section we used periodic boundary conditions and a cooling rate of 1.5×10^5 K/s, and initialized the system as a uniform liquid.

Figure 7 shows the nucleation and subsequent time evolution of a polycrystalline network of grains in a binary alloy, starting from a liquid state and with thermal fluctuations applied over time. Time goes from left to right as the corresponding undercooling (Δ) grows. The rows display the concentration field and different measures of the vector order parameter. The data show that the thermal fluctuations grow over time as the driving force increases, leading to homogeneous nucleation of globular structures, i.e., the nuclei, as shown in the first column of Fig. 7. The nuclei then start to merge and coalesce into a polycrystalline network, which starts to coarsen over time. The grain boundaries in this set of simulations appear jagged and noisy due to thermal fluctuations, but eventually do smooth out (coarsen) due to surface energy minimization at later times.

It should be noted that there is some ambiguity about how to interpret the effect of using an artificially stretched computational interface width (here $W_0 = d_0/0.277 \approx 44$ nm) on nucleation events in any phase field simulation. A working interpretation is that for a W_0 that is artificially stretched the phase field “nuclei” that emerge represent, loosely, a crystal “mass” that is actually the collective fusion of many

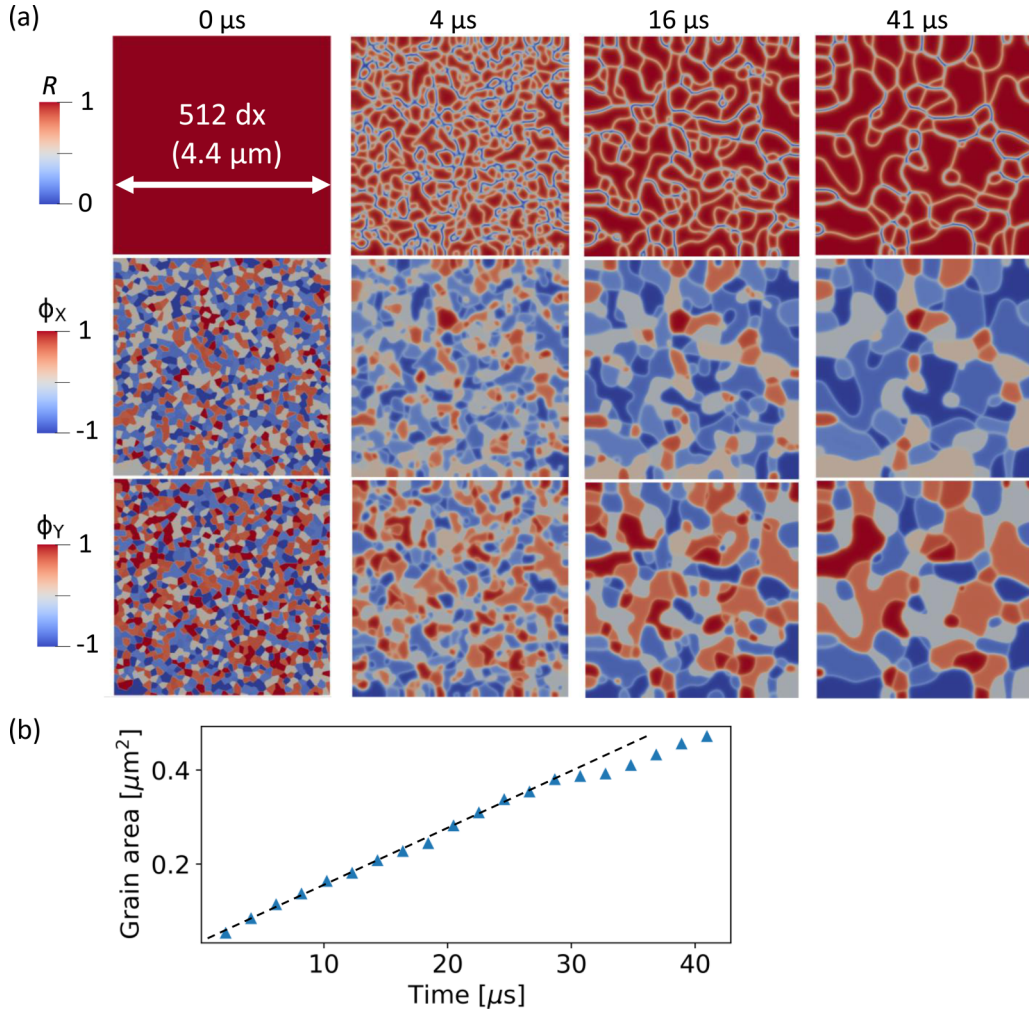


FIG. 6. Polycrystalline coarsening using the proposed vector order parameter model, constrained to model A (no solute dynamics), with an undercooling of $\Delta = 0.55$ and solid-solid barrier $b = 4.0$. (a) Time evolution of the polycrystalline grain network, where time increases from left to right. The rows show different measures of the order parameter. (b) Solid fraction vs time, with the linear scaling regime shown by the dashed line as a guide for the eye.

nanometer-scale nuclei formed over the coarse-grained volume W_0^d and over the coarse-grained time scale τ_0 . In other words, if we imagine coarse-graining solidification microstructure on length and time scales much larger than W_0 and τ_0 , respectively, such a “supernucleus” can be then seen as what emerges from the spatial and temporal coarse graining of the microscopic nucleation process.

IV. DISCUSSION

In the proposed vector order parameter phase field model, the number of solid wells, i.e., the number of unique grains, can be practically limited to a number of order $N_{\text{wells}} \sim 10$ due to numerical resolution issues. This is in contrast to the phase field models that use a continuous orientation field [4–6], where the possible crystal orientations are not restricted to discrete values, although numerical resolution will ultimately limit the total number of orientations that even such models can practically realize in simulations. However, the number of solid wells (unique orientations) can be increased easily if the grid spacing Δx is decreased. A more practical and simple

technique for increasing the number of grains that avoids the excessive computational cost associated with decreasing Δx would be to increase the vector order parameter dimensionality from $d = 2$ (ϕ_x and ϕ_y) to, e.g., $d = 3$ or 4 (ϕ_K , $K = 1, \dots, d$).

The solid wells in the energy landscape defined by the vector order parameter can also be used to represent multiple thermodynamically distinct solid phases. Here, the aforementioned increase of vector order parameter dimensionality could be used to assign different solid wells to different phases. In our preliminary tests using the local supersaturation approximation [12,24], the number of solid wells (N_{wells}) needs to be rather small to describe phases with notably different solubilities, such as an α fcc aluminium phase and an intermetallic Al_2Cu phase.

In order to reduce computational costs associated with the use of multiple order parameters to represent distinct phases, multiphase field model or multi-order-parameter phase field models can use so-called reindexing algorithms as a way to reassign grains to avoid artificial melding of neighboring grains [10]. This reindexing might not be possible for the

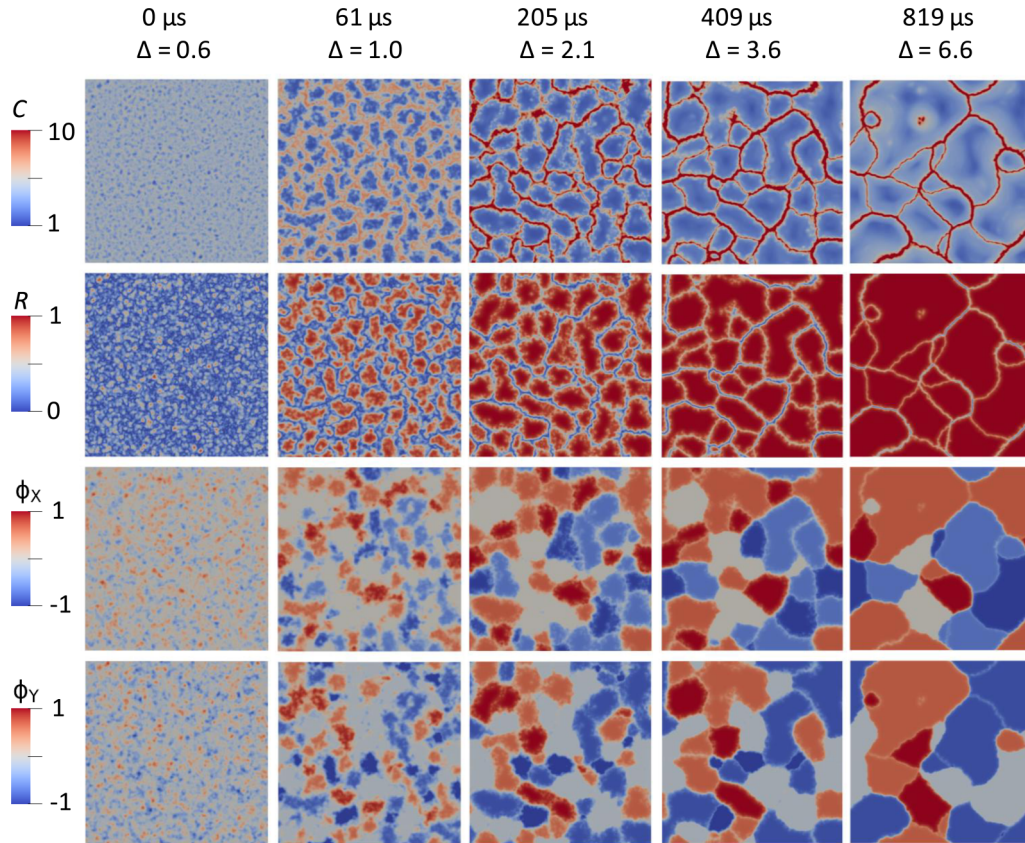


FIG. 7. Thermally induced homogeneous nucleation, polycrystalline solidification, and coarsening in a binary alloy simulated with the proposed vector order parameter phase field model. Model parameters are taken from Table I ($\Delta x = 0.2W_0$). The cooling rate is set to 1.5×10^5 K/s. Time flows from left to right as the corresponding undercooling increases. The rows indicate the fields of the model.

current vector order parameter model, as the order parameters of neighboring grains are directly interacting with each other and relax to profiles such as those shown in Fig. 3. However, the use of higher dimensional vector order parameter fields, coupled with adaptive mesh refinement, should be able to provide ample degrees of freedom to simulate polycrystalline networks relatively efficiently in the context of a single physical order parameter.

The anisotropy of grain boundaries can be an important feature in polycrystalline coarsening, characterized in three dimensions by three misorientation angles and two inclination angles [25]—in a 2D system by two misorientation angles and a single inclination angle. In its current form, the present model depends mostly on the misorientation, i.e., on which solid wells are in contact. There is a minor inclination dependence through the anisotropic solid-liquid interface energy. We expect that the inclination dependence can be increased by, for example, adding an anisotropic energy term proportional to $|\theta|^2$ for the energy expression in Eq. (6), analogously to how it is done for the solid-liquid interface energy.

Physically, grain boundaries move significantly slower than the solid-liquid interface. As grain boundaries are necessarily associated with a change in orientation, the mobility decrease could be implemented by adding an orientation gradient $|\nabla\theta|^2$ dependence to the phase field time scale, for example in the form $\tau_K \rightarrow [1 - \exp(-A|\nabla\theta|^2)]\tau_K$, where

A controls how strongly the mobility decays around grain boundaries.

Numerically, the present vector order parameter model requires a somewhat denser grid than traditional phase field models, with roughly $\Delta x \sim 0.2W_0$ (compared to $\Delta x \sim 0.4W_0$ used typically), in order to resolve the grain boundary profiles and to avoid mesh pinning. This becomes more arduous when the driving force or undercooling is increased since this leads to steeper profiles, a feature, however, that is also present to some extent in all phase field models. This requires further investigation to find possible numerical remedies. It is noted, however, that the necessity for a relatively dense grid is counterbalanced by the fact that this vector order parameter model requires only a small number of equations to describe the order parameter evolution, in contrast to multi-order-parameter models [3] or multiphase field models [1], which require 10–20 evolution equations. Rigorous analysis comparing the numerical efficiency of this vector order parameter model to other polycrystalline phase field models is a topic that should be investigated in the future.

In closing, it is noted that the vector order parameter model can be more elegantly formulated in polar coordinates R and θ (see Fig. 1). However, in our tests, the system is prone to mesh pinning due to topological defects analogous to those seen by Korbuly *et al.* [7] for the orientation phase field model. For those readers interested in pursuing this formulation, Korbuly *et al.* present techniques and remedies to address these

issues that are expected to also be applicable to the present model.

V. CONCLUSION

The vector order parameter phase field model presented in this paper is introduced as a practical tool for the study of microstructure evolution in polycrystalline solidification, and which reproduces key benchmarks quantitatively. The specific benchmarks that were demonstrated in this paper are dendrite solidification [15,16], grain boundary energy versus misorientation and undercooling, coalescence and segregation associated with back-diffusion, and nucleation-induced solidification and coarsening in binary alloys.

Future work with this vector order parameter phase field model will explore the addition of higher dimensional vector order parameter fields in order to increase the efficiency increasing the number of unique grains, and to introduce new thermodynamically distinct phases, thus making possible the efficient simulation of multiphase solidification, such as for example the simulation of intermetallic phases in the Al-Cu system.

ACKNOWLEDGMENTS

N.P. acknowledges the National Science and Engineering Research Council of Canada (NSERC) and the Canada Research Chairs (CRC) Program. T.P. and A.L. acknowledge the support of Academy of Finland through the HEADFORE project, Grant No. 333226.

APPENDIX: VARIATIONAL DERIVATIVE OF THE INTERFACE ENERGY TERM

This section shows the explicit expression for the interface energy term for the vector order parameter model, Eq. (5). Let us first separate the anisotropy function from interface width as $W_K = W_0 a_K$. Then the gradient penalty free energy contribution for the order parameter model is

$$\int_V f_{\text{int}} dV = \int_V \sum_{K=X,Y} W_0^2 \frac{1}{2} |a_K(\theta_{\nabla\phi_K}, \theta) \nabla\phi_K|^2 dV, \quad (\text{A1})$$

where

$$a_K(\phi_X, \phi_Y, \nabla\phi_K) = 1 + \epsilon_c \cos(4\theta_{\nabla\phi_K} - \theta), \quad (\text{A2})$$

where the local interface normal angle is

$$\theta_{\nabla\phi_K} = \arctan\left(\frac{\partial_y\phi_K}{\partial_x\phi_K}\right), \quad (\text{A3})$$

and the reference angle of order parameter vector $\vec{\phi} = (\phi_X, \phi_Y)$ is

$$\theta = \arctan\left(\frac{\phi_Y}{\phi_X}\right). \quad (\text{A4})$$

For order parameter vector components $K \in \{X, Y\}$, the total variational derivative of this term is then

$$\begin{aligned} \frac{\delta}{\delta\phi_K} \left(\sum_{K'=X,Y} \frac{1}{2} |a_{K'} \nabla\phi_{K'}|^2 \right) &= \left(\frac{\partial}{\partial\phi_K} - \nabla \times \frac{\partial}{\partial\nabla\phi_K} \right) \left(\sum_{K'=X,Y} \frac{1}{2} |a_{K'} \nabla\phi_{K'}|^2 \right) \\ &= a_X \frac{\partial a_X}{\partial\phi_K} |\nabla\phi_X|^2 + a_Y \frac{\partial a_Y}{\partial\phi_K} |\nabla\phi_Y|^2 \\ &\quad - \nabla \left(a_K^2 \nabla\phi_K + a_K |\nabla\phi_K|^2 \frac{\partial a_K}{\partial\nabla\phi_K} \right), \end{aligned} \quad (\text{A5})$$

where $\frac{\partial}{\partial\nabla\phi_K} := \sum_i^{x,y,z} \hat{e}_i \frac{\partial}{\partial(\partial_i\phi_K)}$, and the following identities are used:

$$\frac{\partial\theta}{\partial\phi_X} = -\frac{\phi_Y}{|\phi|^2}, \quad \frac{\partial\theta}{\partial\phi_Y} = \frac{\phi_X}{|\phi|^2}, \quad (\text{A6})$$

$$\frac{\partial\theta_{\nabla\phi_K}}{\partial(\partial_x\phi_K)} = -\frac{\partial_y\phi_K}{|\nabla\phi_K|^2}, \quad \frac{\partial\theta_{\nabla\phi_K}}{\partial(\partial_x\phi_K)} = \frac{\partial_x\phi_K}{|\nabla\phi_K|^2}, \quad (\text{A7})$$

$$a'_K(\theta_{\nabla\phi_K}, \theta) = -4\epsilon_c \sin(4\theta_{\nabla\phi_K} - \theta), \quad (\text{A8})$$

$$\begin{aligned} \frac{\partial a_K}{\partial(\partial_x\phi_K)} &= a'_K(\theta_{\nabla\phi_K}, \theta) \frac{\partial\theta_{\nabla\phi_K}}{\partial(\partial_x\phi_K)} \\ &= -a'_K(\theta_{\nabla\phi_K}, \theta) \frac{\partial_y\phi_K}{|\nabla\phi_K|^2}, \end{aligned} \quad (\text{A9})$$

$$\begin{aligned} \frac{\partial a_K}{\partial(\partial_y\phi_K)} &= a'_K(\theta_{\nabla\phi_K}, \theta) \frac{\partial\theta_{\nabla\phi_K}}{\partial(\partial_y\phi_K)} \\ &= a'_K(\theta_{\nabla\phi_K}, \theta) \frac{\partial_x\phi_K}{|\nabla\phi_K|^2}, \end{aligned} \quad (\text{A10})$$

$$\begin{aligned} \frac{\partial a_K}{\partial\phi_K} &= \epsilon_c \sin(4\theta_{\nabla\phi_K} - \theta) \frac{\partial\theta}{\partial\phi_K} \\ &= -\frac{1}{4} a'_K(\theta_{\nabla\phi_K}, \theta) \frac{\partial\theta}{\partial\phi_K}. \end{aligned} \quad (\text{A11})$$

-
- [1] I. Steinbach and F. Pezzolla, A generalized field method for multiphase transformations using interface fields, *Physica D* **134**, 385 (1999).
- [2] B. Bottger, J. Eiken, and I. Steinbach, Phase field simulation of equiaxed solidification in technical alloys, *Acta Mater.* **54**, 2697 (2006).
- [3] N. Ofori-Opoku and N. Provatas, A quantitative multi-phase field model of polycrystalline alloy solidification, *Acta Mater.* **58**, 2155 (2010).
- [4] R. Kobayashi, J. A. Warren, and W. C. Carter, Vector-valued phase field model for crystallization and grain boundary formation, *Physica D* **119**, 415 (1998).
- [5] L. Gránásy, T. Börzsönyi, and T. Pusztai, Crystal nucleation and growth in binary phase-field theory, *J. Cryst. Growth* **237**, 1813 (2002).
- [6] J. A. Warren, R. Kobayashi, A. E. Lobkovsky, and W. C. Carter, Extending phase field models of solidification to polycrystalline materials, *Acta Mater.* **51**, 6035 (2003).

- [7] B. Korbuly, M. Plapp, H. Henry, J. A. Warren, L. Gránásy, and T. Pusztai, Topological defects in two-dimensional orientation-field models for grain growth, *Phys. Rev. E* **96**, 052802 (2017).
- [8] T. Pusztai, G. Bortel, and L. Gránásy, Phase field theory of polycrystalline solidification in three dimensions, *Europhys. Lett.* **71**, 131 (2005).
- [9] H. Salama, J. Kundin, O. Shchyglo, V. Mohles, K. Marquardt, and I. Steinbach, Role of inclination dependence of grain boundary energy on the microstructure evolution during grain growth, *Acta Mater.* **188**, 641 (2020).
- [10] C. E. K. III and L.-Q. Chen, Computer simulation of 3-D grain growth using a phase-field model, *Acta Mater.* **50**, 3059 (2002).
- [11] B. Morin, K. R. Elder, M. Sutton, and M. Grant, Model of the Kinetics of Polymorphous Crystallization, *Phys. Rev. Lett.* **75**, 2156 (1995).
- [12] M. Plapp, Unified derivation of phase-field models for alloy solidification from a grand-potential functional, *Phys. Rev. E* **84**, 031601 (2011).
- [13] N. Provatas and K. Elder, *Phase-Field Methods in Materials Science and Engineering* (Wiley, New York, 2010).
- [14] A. A. Wheeler, W. J. Boettinger, and G. B. McFadden, Phase-field model for isothermal phase transitions in binary alloys, *Phys. Rev. A* **45**, 7424 (1992).
- [15] A. Karma, Phase-field Formulation for Quantitative Modeling of Alloy Solidification, *Phys. Rev. Lett.* **87**, 115701 (2001).
- [16] B. Echebarria, R. Folch, A. Karma, and M. Plapp, Quantitative phase-field model of alloy solidification, *Phys. Rev. E* **70**, 061604 (2004).
- [17] A. Karma and W. J. Rappel, Quantitative phase-field modeling of dendritic growth in two and three dimensions, *Phys. Rev. E* **57**, 4323 (1998).
- [18] R. Almgren, Second-order phase field asymptotics for unequal conductivities, *SIAM J. Appl. Math.* **59**, 2086 (1999).
- [19] A. Karma and W.-J. Rappel, Phase-field model of dendritic sidebranching with thermal noise, *Phys. Rev. E* **60**, 3614 (1999).
- [20] See Supplemental Material at <http://link.aps.org/supplemental/10.1103/PhysRevE.103.053310> for a finite volume expression of the interface energy penalty, analytical grain boundary energy estimates, spatial and temporal filtering of the thermal noise, and polycrystalline coarsening using a small solid-solid barrier parameter.
- [21] M. Greenwood, K. Shampur, N. Ofori-Opoku, T. Pinomaa, L. Wang, S. Gurevich, and N. Provatas, Quantitative 3D phase field modelling of solidification using next-generation adaptive mesh refinement, *Comput. Mater. Sci.* **142**, 153 (2018).
- [22] J. Mellenthin, A. Karma, and M. Plapp, Phase-field crystal study of grain-boundary premelting, *Phys. Rev. B* **78**, 184110 (2008).
- [23] M. Rappaz, A. Jacot, and W. J. Boettinger, Last-stage solidification of alloys: theoretical model of dendrite-arm and grain coalescence, *Metall. Mater. Trans. A* **34**, 467 (2003).
- [24] K. Shampur, A grand potential based multi-phase field model for alloy solidification, Master's thesis, McGill University, 2017.
- [25] G. S. Rohrer, Grain boundary energy anisotropy: A review, *J. Mater. Sci.* **46**, 5881 (2011).